

Fiber Enhancement in Diffusion-Weighted MRI

Remco Duits^{1,2}, Tom C.J. Dela Haije², Arpan Ghosh¹, Eric Creusen^{1,2},
Anna Vilanova², and Bart ter Haar Romeny²

Eindhoven University of Technology, The Netherlands,

¹ Department of Mathematics and Computer Science

² Department of Biomedical Engineering

{R.Duits,A.Ghosh,E.J.Creusen,B.M.terhaarRomeny,A.Vilanova}@tue.nl,
T.C.J.Dela.Haije@student.tue.nl

Abstract. Diffusion-Weighted MRI (DW-MRI) measures local water diffusion in biological tissue, which reflects the underlying fiber structure. In order to enhance the fiber structure in the DW-MRI data we consider both (convection-)diffusions and Hamilton-Jacobi equations (erosions) on the space $\mathbb{R}^3 \times S^2$ of 3D-positions and orientations, embedded as a quotient in the group $SE(3)$ of 3D-rigid body movements. These left-invariant evolutions are expressed in the frame of left-invariant vector fields on $SE(3)$, which serves as a moving frame of reference attached to fiber fragments. The linear (convection-)diffusions are solved by a convolution with the corresponding Green's function, whereas the Hamilton-Jacobi equations are solved by a morphological convolution with the corresponding Green's function. Furthermore, we combine dilation and diffusion in pseudo-linear scale spaces on $\mathbb{R}^3 \times S^2$. All methods are tested on DTI-images of the brain. These experiments indicate that our techniques are useful to deal with both the problem of limited angular resolution of DTI and the problem of spurious, non-aligned crossings in HARDI.

Keywords: DTI, HARDI, DW-MRI, sub-Riemannian geometry, scale spaces, Lie groups, Hamilton-Jacobi equations, erosion.

1 Introduction

Diffusion-Weighted Magnetic Resonance Imaging (DW-MRI) involves magnetic resonance techniques for non-invasively measuring local water diffusion in tissue. Local water diffusion profiles reflect underlying biological fiber structure. For instance in the brain, diffusion is less constrained parallel to nerve fibers than perpendicular to them.

The diffusion of water molecules in tissue over time t is described by a transition density function p_t , cf. [2]. Diffusion Tensor Imaging (DTI), introduced by Basser et al. [3], assumes that p_t can be described for each position $\mathbf{y} \in \mathbb{R}^3$ by an anisotropic Gaussian. If $\{Y_t\}$ denotes the stochastic process describing the movement of water-molecules in \mathbb{R}^3 , then one has

$$p_t(Y_t = \mathbf{y}' \mid Y_0 = \mathbf{y}) = (4\pi t)^{-\frac{3}{2}} |\det(D(\mathbf{y}))|^{-\frac{1}{2}} e^{-\frac{(\mathbf{y}' - \mathbf{y})^T (D(\mathbf{y}))^{-1} (\mathbf{y}' - \mathbf{y})}{4t}},$$

where D is a tensor field of positive definite symmetric tensors on \mathbb{R}^3 estimated from the MRI data. In a DTI-visualization one plots the surfaces

$$\mathbf{y} + \{\mathbf{v} \in \mathbb{R}^3 \mid \mathbf{v}^T D^{-1}(\mathbf{y}) \mathbf{v} = \mu^2\}, \quad (1)$$

where $\mu > 0$ is fixed and $\mathbf{y} \in \Omega$ with Ω some compact subset of \mathbb{R}^3 . From now on we refer to these surfaces as DTI-glyphs.

The drawback of this anisotropic Gaussian function approximation is the limited angular resolution of the corresponding probability density $U : \mathbb{R}^3 \times S^2 \rightarrow \mathbb{R}^+$ on positions and orientations

$$U(\mathbf{y}, \mathbf{n}) = \frac{3}{4\pi \int_{\Omega} \text{trace}\{D(\mathbf{y}')\} d\mathbf{y}'} \mathbf{n}^T D(\mathbf{y}) \mathbf{n}, \quad \mathbf{y} \in \mathbb{R}^3, \mathbf{n} \in S^2. \quad (2)$$

Thereby unprocessed DTI is not capable of representing crossing fibers [2].

High Angular Resolution Diffusion Imaging (HARDI) is another recent DW-MRI technique for imaging water diffusion processes in fibrous tissues. HARDI provides for each position in \mathbb{R}^3 and for each orientation in S^2 an MRI signal attenuation profile, which can be related to the local diffusivity of water molecules in the corresponding direction. As a result, HARDI images are distributions $(\mathbf{y}, \mathbf{n}) \mapsto U(\mathbf{y}, \mathbf{n})$ over positions and orientations. HARDI is not restricted to functions on S^2 induced by a quadratic form and is thus capable of reflecting crossing information. See Fig. 1, where a HARDI data set is depicted using glyph visualization as defined below. In HARDI modeling the Fourier transform of the estimated transition densities is typically considered at a fixed characteristic radius (generally known as the *b-value*), cf. [8].

Definition 1. A *glyph* of a distribution $U : \mathbb{R}^3 \times S^2 \rightarrow \mathbb{R}^+$ on positions and orientations is a surface $\mathcal{S}_\mu(U)(\mathbf{y}) = \{\mathbf{y} + \mu U(\mathbf{y}, \mathbf{n}) \mathbf{n} \mid \mathbf{n} \in S^2\} \subset \mathbb{R}^3$ for some $\mathbf{y} \in \mathbb{R}^3$, and some suitably chosen $\mu > 0$. A *glyph visualization* of the distribution $U : \mathbb{R}^3 \times S^2 \rightarrow \mathbb{R}^+$ is a visualization of a field $\mathbf{y} \mapsto \mathcal{S}_\mu(U)(\mathbf{y})$ of glyphs.

For the purpose of detecting and visualizing biological fibers, DTI and HARDI data should be enhanced by fiber propagation models such that fiber junctions are more visible and high frequency noise and non-aligned glyphs are reduced. Promising research has been done on constructing diffusion/regularization processes on the 2-sphere defined at each spatial locus separately [8,13] as an essential pre-processing step for robust fiber tracking. In these approaches position- and orientation space are decoupled, and diffusion is only performed over the angular part, disregarding spatial context. Consequently, these methods tend to fail precisely at the interesting locations where fibres cross or bifurcate.

In contrast to previous work on enhancement of DW-MRI [8,13,15,5], we consider both the spatial and the orientational part to be included in the *domain*, so a HARDI dataset is considered as a function $U : \mathbb{R}^3 \times S^2 \rightarrow \mathbb{R}^+$. Furthermore, we explicitly employ the proper underlying group structure, that arises by embedding the coupled space of positions and orientations

$$\mathbb{R}^3 \times S^2 := SE(3)/(\{0\} \times SO(2))$$

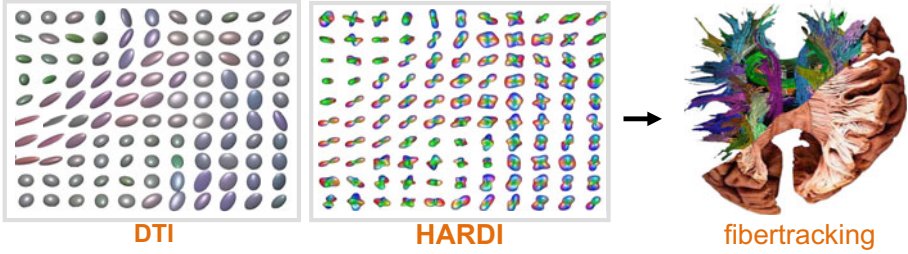


Fig. 1. This figure shows glyph visualizations of HARDI and DTI-images of a 2D-slice in the brain where neural fibers in the corona radiata cross with neural fibers in the corpus callosum. Here DTI and HARDI are visualized differently; HARDI is visualized according to Def. 1, whereas DTI is visualized using Eq. (1).

as the partition of left cosets into the group $SE(3) = \mathbb{R}^3 \rtimes SO(3)$ of 3D-rigid motions. The group product on $SE(3)$ is given by

$$(\mathbf{x}, R)(\mathbf{x}', R') = (\mathbf{x} + R\mathbf{x}', RR'),$$

for all positions $\mathbf{x}, \mathbf{x}' \in \mathbb{R}^3$ and rotations $R, R' \in SO(3)$. Throughout this article we use the following identification between the DW-MRI image $(\mathbf{y}, \mathbf{n}) \rightarrow U(\mathbf{y}, \mathbf{n})$ and functions $\tilde{U}: SE(3) \rightarrow \mathbb{R}$ given by

$$\tilde{U}(\mathbf{y}, R) = U(\mathbf{y}, R\mathbf{e}_z) \text{ with } \mathbf{e}_z = (0, 0, 1)^T. \quad (3)$$

The general advantage of our approach on $SE(3)$ is that we can enhance the original HARDI/DTI data using orientational and spatial neighborhood information simultaneously. This can create crossings in DTI data and allows a reduction of scanning directions in areas where the random walks that underly (hypo-elliptic) diffusion [11, ch:4.2] on $\mathbb{R}^3 \rtimes S^2$ yield reasonable fiber extrapolations, cf. [11,19,18] and see Fig. 2. HARDI already produces more detailed information about complex-fiber structures. Application of the same (hypo-elliptic) diffusion on HARDI then removes spurious crossings, see Fig. 3 and [19]. Here we will address the following issues that arise from our previous work [18,11,19]:

- Can we replace the grey-scale transformations [18,11,19] by Hamilton-Jacobi equations (erosions) on $\mathbb{R}^3 \rtimes S^2$ to visually sharpen the fibers in the data?
- Can we find the viscosity solutions of these Hamilton-Jacobi equations?
- Can we find analytic approximations for the viscosity solutions of these left-invariant Hamilton-Jacobi equations on $\mathbb{R}^3 \rtimes S^2$, similar to the analytic approximations of the linear left-invariant diffusions, cf. [11, ch:6.2]?
- Can we combine left-invariant diffusions and left-invariant dilations in a pseudo-linear scale space on $\mathbb{R}^3 \rtimes S^2$, generalizing [14] to DW-MRI images?

To address these issues, we introduce besides linear scale spaces, morphological and pseudo-linear scale spaces, all defined on $(\mathbb{R}^3 \rtimes S^2) \times \mathbb{R}^+$:

$$(\mathbf{y}, \mathbf{n}, t) \mapsto W(\mathbf{y}, \mathbf{n}, t) \text{ for all } \mathbf{y} \in \mathbb{R}^3, \mathbf{n} \in S^2, t > 0,$$

where the input DW-MRI image serves as initial condition $W(\mathbf{y}, \mathbf{n}, 0) = U(\mathbf{y}, \mathbf{n})$.

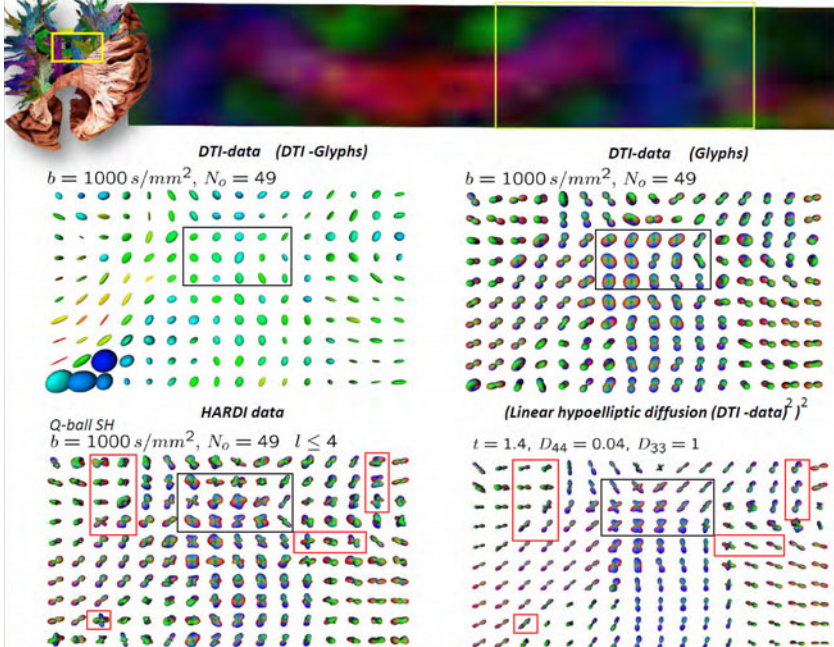


Fig. 2. DTI and HARDI data containing fibers of the corpus callosum and the corona radiata in a human brain, with b -value 1000 s/mm^2 on voxels of $(2\text{mm})^3$, cf. [18]. We visualize a 10×16 -slice of interest (162 samples on S^2 using icosahedron tessellations) from $104 \times 104 \times 10 \times (162 \times 3)$ datasets. Top row: region of interest with fractional anisotropy intensities with colorcoded DTI-principal directions. Middle row, DTI data U visualized according to Eq.(1) resp. Def. 1. Bottom row: HARDI data (Q-ball with $l \leq 4$, [8]) of the same region, hypo-elliptically diffused DTI data $(y, n) \mapsto W(y, n, t)$, Eq. (9). We applied min-max normalization of $W(y, \cdot, t)$ for all positions y .

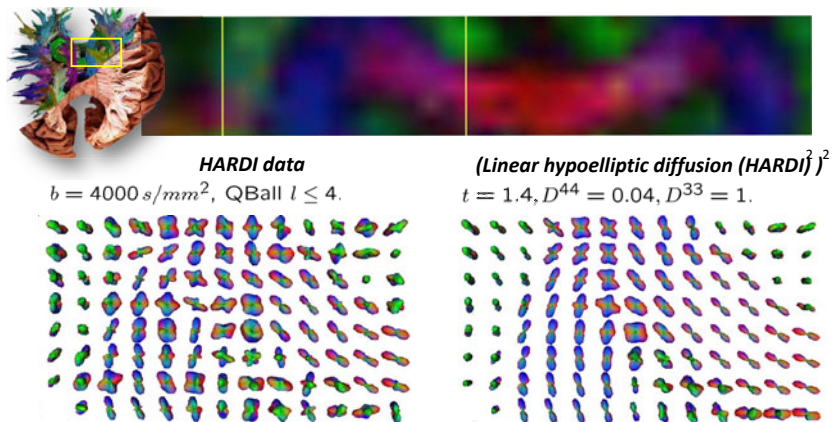


Fig. 3. Same settings as Fig:2, except for a different b -value and region of interest. The (hypo-elliptic) diffusion, Eq. (9), is applied to the HARDI dataset.

To get a preview of how these evolutions perform on the same neural DTI dataset (different slice) considered in [18], see Fig. 4, where we used

$$\mathcal{V}(U)(\mathbf{y}, \mathbf{n}) = \left(\frac{U(\mathbf{y}, \mathbf{n}) - U_{min}(\mathbf{y})}{U_{max}(\mathbf{y}) - U_{min}(\mathbf{y})} \right)^2, \text{ with } U_{max}(\mathbf{y}) = \max_{\mathbf{n}} \{U(\mathbf{y}, \mathbf{n}) \mid \mathbf{n} \in S^2\}. \quad (4)$$

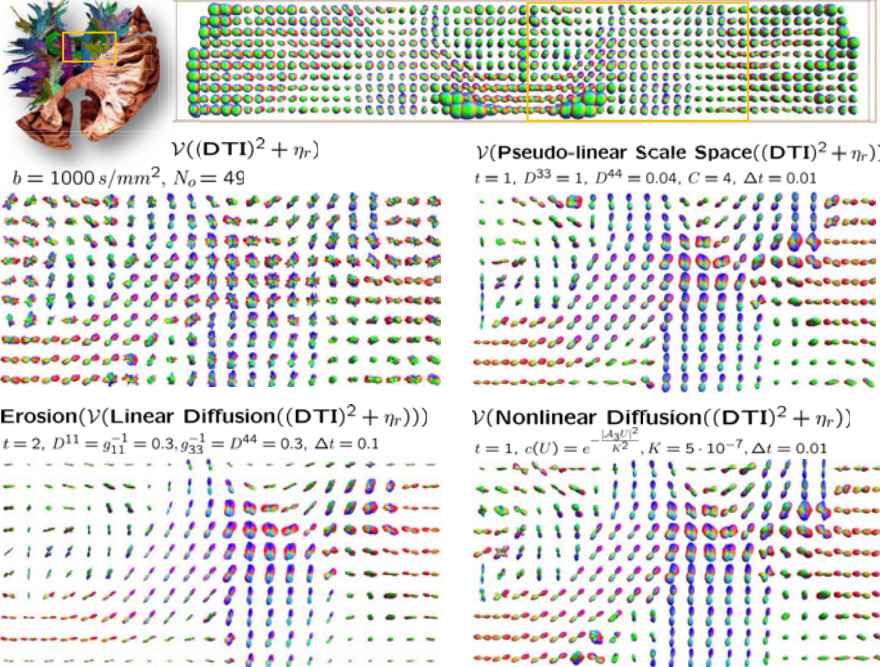


Fig. 4. DTI data of corpus callosum and corona radiata fibers in a human brain with b -value $1000 s/mm^2$ on voxels of $(2mm)^3$. Top row: DTI-visualization according to Eq. (1). The yellow box contains $13 \times 22 \times 10$ glyphs with 162 orientations of the input DTI-data depicted in the left image of the middle row. This input-DTI image U is visualized using Eq. (2) and Rician noise η_r [11, Eq. 90] with $\sigma = 10^{-4}$ has been included. Operator \mathcal{V} is defined in Eq. (4). Middle row, right: output of pseudo-linear scale space, Eq. (12). Bottom row, left: output erosion, Eq. (11) using the diffused DTI-data set as input, Eq. (9) with $(D^{44} = 0.04, D^{33} = 1, t = 1)$, right: output of non-linear diffusions with adaptive scalar diffusivity explained in our companion work [7]. All evolutions are implemented by finite difference schemes, [9], with step size Δt .

1.1 Motivation for Morphological Scale Spaces on $\mathbb{R}^3 \times S^2$

Typically, if linear diffusions are directly applied to DTI the fibers visible in DTI are propagated in too many directions. Therefore we combined these diffusions with monotonic transformations in the codomain \mathbb{R}^+ , such as squaring input and output cf. [11,19,18]. Visually, this produces anatomically plausible results, cf. Fig. 2

and Fig. 3, but does not allow large global variations in the data. This is often problematic around ventricle areas in the brain, where the glyphs are usually larger than those along the fibers as can be seen in the top row of Fig. 4. In order to achieve a better way of sharpening the data where global maxima do not dominate the sharpening of the data, cf. Fig. 5, we propose morphological scale spaces on $\mathbb{R}^3 \times S^2$ where transport takes place orthogonal to the fibers, both spatially and spherically, see Fig. 7. The result of such an erosion after application of a linear diffusion is depicted down left in Fig. 4, where the diffusion has created crossings in the fibers and where the erosion has visually sharpened the fibers.

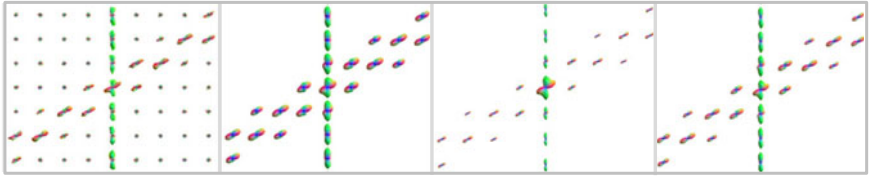


Fig. 5. From left to right. Noisy artificial dataset, output diffused dataset (thresholded), squared output diffused dataset as in [18,11,19], $\mathbb{R}^3 \times S^2$ -eroded output, Eq.(11), diffused dataset, Eq. (9).

2 A Moving Frame of Reference for Scale Spaces on $\mathbb{R}^3 \times S^2$

Evolutions on DW-MRI must commute with rotations and translations. Therefore our evolutions on DW-MRI and the underlying metric-tensor are expressed in a local frame of reference attached to fiber fragments. This frame of reference $\{\mathcal{A}_1, \dots, \mathcal{A}_6\}$ consists of 6 left-invariant vector fields on $SE(3)$ given by

$$\mathcal{A}_i \tilde{U}(\mathbf{y}, R) = \lim_{h \downarrow 0} \frac{\tilde{U}((\mathbf{y}, R) e^{h \mathcal{A}_i}) - \tilde{U}((\mathbf{y}, R) e^{-h \mathcal{A}_i})}{2h} \quad (5)$$

where $\{A_1, \dots, A_6\}$ is the basis for the Lie-algebra at the unity element and $T_e(SE(3)) \ni A \mapsto e^A \in SE(3)$ is the exponential map in $SE(3)$. For more explicit, non-trivial, analytical formulas of the exponential map and corresponding left-invariant vector fields (5) we refer to [11, ch:3.3, Eq. 23–25, ch:5.1 Eq. 54]. However, these technical formulas are only needed for analytic approximation of Green’s functions, see [11, ch:6]. In practice one uses finite difference approximations [11, ch:7], where spherical interpolation in between higher order tessellation of the icosahedron can be done by means of the discrete spherical harmonic transform [11, ch:7.1] or by triangular interpolation [7]. For an intuitive preview of this moving frame of reference attached to points in $\mathbb{R}^3 \times S^2 = (SE(3)/(\{0\} \times SO(2)))$ we refer to Fig. 7.

The associated left-invariant dual frame $\{d\mathcal{A}^1, \dots, d\mathcal{A}^6\}$ is determined by

$$\langle d\mathcal{A}^i, \mathcal{A}_j \rangle := d\mathcal{A}^i(\mathcal{A}_j) = \delta_j^i, i, j = 1, \dots, 6, \quad (6)$$

where $\delta_j^i = 1$ if $i = j$ and zero else. Then all possible left-invariant metric tensors on $SE(3)$ are given by $\mathbf{G}_{(\mathbf{y}, R_{\mathbf{n}})} = \sum_{i,j=1}^6 g_{ij} d\mathcal{A}^i|_{(\mathbf{y}, R_{\mathbf{n}})} \otimes d\mathcal{A}^j|_{(\mathbf{y}, R_{\mathbf{n}})}$ with $g_{ij} \in \mathbb{C}$ and where $\mathbf{y} \in \mathbb{R}^3$, $\mathbf{n} \in S^2$, and where $R_{\mathbf{n}} \in SO(3)$ is *any* rotation that maps \mathbf{e}_z onto the normal $\mathbf{n} \in S^2$, i.e.

$$R_{\mathbf{n}} \mathbf{e}_z = \mathbf{n}. \quad (7)$$

Necessary and sufficient conditions on g_{ij} to induce a well-defined left-invariant metric on $\mathbb{R}^3 \rtimes S^2$ are derived in [9, App.E]. It turns out that the matrix $[g_{ij}]$ must be constant and diagonal $g_{ij} = \frac{1}{D^{ii}} \delta_{ij}$, $i, j = 1 \dots, 6$ with $D^{ii} \in \mathbb{R}^+ \cup \infty$, with $D^{11} = D^{22}$, $D^{44} = D^{55}$, $D^{66} = 0$. The metric is thereby parameterized by the values of D^{11}, D^{33} and D^{44} , and we write the metric as a tensor product of left-invariant co-vectors:

$$\mathbf{G} = \frac{1}{D^{11}} (d\mathcal{A}^1 \otimes d\mathcal{A}^1 + d\mathcal{A}^2 \otimes d\mathcal{A}^2) + \frac{1}{D^{33}} (d\mathcal{A}^3 \otimes d\mathcal{A}^3) + \frac{1}{D^{44}} (d\mathcal{A}^4 \otimes d\mathcal{A}^4 + d\mathcal{A}^5 \otimes d\mathcal{A}^5)$$

The metric tensor on the quotient $\mathbb{R}^3 \rtimes S^2 = (SE(3)/(\{0\} \times SO(2)))$ now reads

$$\mathbf{G}_{(\mathbf{y}, \mathbf{n})} \left(\sum_{i=1}^5 c^i \mathcal{A}_i|_{(\mathbf{y}, \mathbf{n})}, \sum_{j=1}^5 d^j \mathcal{A}_i|_{(\mathbf{y}, \mathbf{n})} \right) = \frac{c^1 d^1 + c^2 d^2}{D^{11}} + \frac{c^3 d^3}{D^{33}} + \frac{c^4 d^4 + c^5 d^5}{D^{44}}, \quad (8)$$

where vector fields are described by the differential operators on $C^1(\mathbb{R}^3 \times S^2)$:

$$\begin{aligned} (\mathcal{A}_j|_{(\mathbf{y}, \mathbf{n})} U)(\mathbf{y}, \mathbf{n}) &= \lim_{h \rightarrow 0} \frac{U(\mathbf{y} + h R_{\mathbf{n}} \mathbf{e}_j, \mathbf{n}) - U(\mathbf{y} - h R_{\mathbf{n}} \mathbf{e}_j, \mathbf{n})}{2h}, \\ (\mathcal{A}_{3+j}|_{(\mathbf{y}, \mathbf{n})} U)(\mathbf{y}, \mathbf{n}) &= \lim_{h \rightarrow 0} \frac{U(\mathbf{y}, (R_{\mathbf{n}} R_{\mathbf{e}_j, h}) \mathbf{e}_z) - U(\mathbf{y}, (R_{\mathbf{n}} R_{\mathbf{e}_j, -h}) \mathbf{e}_z)}{2h}, \quad j = 1, 2, 3, \end{aligned}$$

where $R_{\mathbf{e}_j, h}$ denotes the counter-clockwise rotation around axis \mathbf{e}_j by angle h , with $\mathbf{e}_1 = (1, 0, 0)^T$, $\mathbf{e}_2 = (0, 1, 0)^T$, $\mathbf{e}_3 = (0, 0, 1)^T$. The induced metric is well-defined on the quotient $\mathbb{R}^3 \rtimes S^2$ since the choice of $R_{\mathbf{n}}$, as defined in Eq.(7), does not matter as the metric tensor is isotropic in the planes depicted in Fig. 7. In the remainder of this article we sometimes use short notation \mathcal{A}_i for $\mathcal{A}_i|_{(\mathbf{y}, \mathbf{n})}$.

3 The Evolution Equations for Scale Spaces on DW-MRI

The spherical and the spatial Laplacian can be expressed in the left-invariant vector fields as $\Delta_{S^2} = (\mathcal{A}_4)^2 + (\mathcal{A}_5)^2$ and $\Delta_{\mathbb{R}^3} = (\mathcal{A}_1)^2 + (\mathcal{A}_2)^2 + (\mathcal{A}_3)^2$. These Laplacians generate diffusion over S^2 and \mathbb{R}^3 separately and are thereby likely to destroy the fiber structure in DW-MRI, [11]. Therefore we introduce the following evolutions (with time $t > 0$) for respectively, linear contour enhancement¹:

$$\begin{cases} \frac{\partial W}{\partial t}(\mathbf{y}, \mathbf{n}, t) = ((D^{33}(\mathcal{A}_3)^2 + D^{44} \Delta_{S^2}) W)(\mathbf{y}, \mathbf{n}, t), \\ W(\mathbf{y}, \mathbf{n}, 0) = U(\mathbf{y}, \mathbf{n}), \end{cases} \quad (9)$$

¹ Eq. (9) boils down to hypo-elliptic diffusion and corresponds to Brownian motion on $\mathbb{R}^3 \rtimes S^2$ [11, ch:4.2], generalizing some of the results in [17,10,4] to 3D.

for linear contour completion²:

$$\begin{cases} \frac{\partial W}{\partial t}(\mathbf{y}, \mathbf{n}, t) = ((-\mathcal{A}_3 + D^{44} \Delta_{S^2}) W)(\mathbf{y}, \mathbf{n}, t), \\ W(\mathbf{y}, \mathbf{n}, 0) = U(\mathbf{y}, \mathbf{n}), \end{cases} \quad (10)$$

and for morphological scale spaces:

$$\begin{cases} \frac{\partial W}{\partial t}(\mathbf{y}, \mathbf{n}, t) = \pm \frac{1}{2\eta} \left(\mathbf{G}_{(\mathbf{y}, \mathbf{n})}^{-1} (\mathrm{d}W(\cdot, \cdot, t)|_{\mathbf{y}, \mathbf{n}}, \mathrm{d}W(\cdot, \cdot, t)|_{\mathbf{y}, \mathbf{n}}) \right)^{\eta} \\ = \pm \frac{1}{2\eta} (D^{11} (|\mathcal{A}_1 W(\mathbf{y}, \mathbf{n}, t)|^2 + |\mathcal{A}_2 W(\mathbf{y}, \mathbf{n}, t)|^2) + \\ D^{44} (|\mathcal{A}_4 W(\mathbf{y}, \mathbf{n}, t)|^2 + |\mathcal{A}_5 W(\mathbf{y}, \mathbf{n}, t)|^2))^{\eta}, \\ W(\mathbf{y}, \mathbf{n}, 0) = U(\mathbf{y}, \mathbf{n}), \end{cases} \quad (11)$$

with $\eta \in [\frac{1}{2}, 1]$, cf. Fig. 6. Finally, for pseudo-linear scale spaces:

$$\begin{cases} \frac{\partial W}{\partial t}(\mathbf{y}, \mathbf{n}, t) = ((D^{33}(\mathcal{A}_3)^2 + D^{44} \Delta_{S^2}) W)(\mathbf{y}, \mathbf{n}, t) + \\ C (D^{33} |\mathcal{A}_3 W(\mathbf{y}, \mathbf{n}, t)|^2 + D^{44} (|\mathcal{A}_4 W(\mathbf{y}, \mathbf{n}, t)|^2 + |\mathcal{A}_5 W(\mathbf{y}, \mathbf{n}, t)|^2)), \\ W(\mathbf{y}, \mathbf{n}, 0) = U(\mathbf{y}, \mathbf{n}), \end{cases} \quad (12)$$

where $C > 0$ balances between infinitesimal dilation and diffusion. These evo-

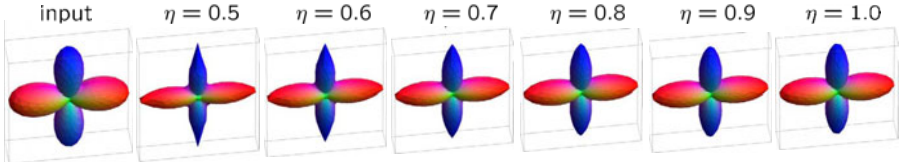


Fig. 6. The effect of $\eta \in [\frac{1}{2}, 1]$ on angular erosion Eq. (11), $D^{44} = 0.4$, $D^{11} = 0$ and $t = 0.4$. Left: original glyph, right eroded glyphs (normalized) for $\eta = 0.5, \dots, 1.0$.

lutions are either solved by (morphological) convolution with the corresponding Green's function or by finite difference schemes. To get an intuition on the underlying geometrical ideas behind these evolutions see Fig. 7.

4 Solving the Evolutions by Convolution on $\mathbb{R}^3 \rtimes S^2$

Operators on DW-MRI data must commute with rotations and translations. This means they must be left-invariant, i.e. they must commute with \mathfrak{L}_g for all $g = (\mathbf{x}, R) \in SE(3)$, where

$$(\mathfrak{L}_g U)(\mathbf{y}, \mathbf{n}) = U(g^{-1} \cdot (\mathbf{y}, \mathbf{n})) = U(R^{-1}(\mathbf{y} - \mathbf{x}), R^{-1}\mathbf{n}),$$

for all $U \in \mathbb{L}_2(\mathbb{R}^3 \rtimes S^2)$, $(\mathbf{y}, \mathbf{n}) \in \mathbb{R}^3 \rtimes S^2$. According to the theorem below, all reasonable linear, left-invariant operators on DW-MRI are $\mathbb{R}^3 \rtimes S^2$ -convolutions.

² Eq. (10) boils down to hypo-elliptic convection-diffusion, direction process on $\mathbb{R}^3 \rtimes S^2$ [11, ch:4.2], generalizing [16,12].

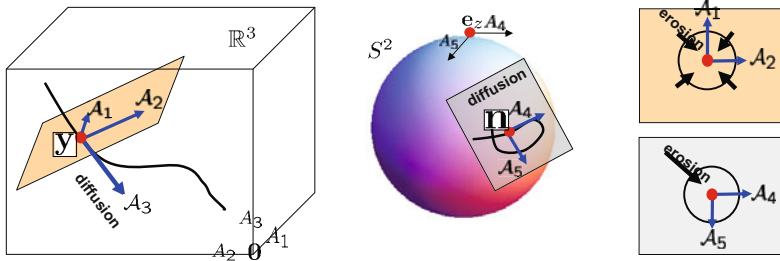


Fig. 7. A curve $[0, 1] \ni s \mapsto \gamma(s) = (\mathbf{x}(s), \mathbf{n}(s)) \rightarrow \mathbb{R}^3 \times S^2$ consists of a spatial part $s \mapsto \mathbf{x}(s)$ (left) and an angular part $s \mapsto \mathbf{n}(s)$ (right). Along this curve we have the moving frame of reference $\{\mathcal{A}_i|_{\tilde{\gamma}(s)}\}_{i=1}^5$ with $\tilde{\gamma}(s) = (\mathbf{x}(s), R_{\mathbf{n}(s)})$ where $R_{\mathbf{n}(s)} \in SO(3)$ is any rotation such that $R_{\mathbf{n}(s)}\mathbf{e}_z = \mathbf{n}(s) \in S^2$. Here \mathcal{A}_i , with $A_i = \mathcal{A}_i|_{(0,I)}$ denote the left-invariant vector fields in $SE(3)$, Eq. (5). To ensure that the diffusions and erosions do not depend on the choice $R_{\mathbf{n}(s)} \in SO(3)$, Eq. (7), these left-invariant evolution equations must be isotropic in the tangent planes $\text{span}\{\mathcal{A}_1, \mathcal{A}_2\}$ and $\text{span}\{\mathcal{A}_4, \mathcal{A}_5\}$. Diffusion/convection primarily takes place along \mathcal{A}_3 in space and (outward) in the plane $\text{span}\{\mathcal{A}_4, \mathcal{A}_5\}$ tangent to S^2 . Erosion takes place both inward in the tangent plane $\text{span}\{\mathcal{A}_1, \mathcal{A}_2\}$ in space and inward in the plane $\text{span}\{\mathcal{A}_4, \mathcal{A}_5\}$.

Theorem 1. Let \mathcal{K} be a bounded operator from $\mathbb{L}_2(\mathbb{R}^3 \times S^2)$ into $\mathbb{L}_\infty(\mathbb{R}^3 \times S^2)$. Then there exists an integrable kernel $k : (\mathbb{R}^3 \times S^2) \times (\mathbb{R}^3 \times S^2) \rightarrow \mathbb{C}$ such that $\|\mathcal{K}\|^2 = \sup_{(\mathbf{y}, \mathbf{n}) \in \mathbb{R}^3 \times S^2} \int_{\mathbb{R}^3 \times S^2} |k(\mathbf{y}, \mathbf{n}; \mathbf{y}', \mathbf{n}')|^2 d\mathbf{y}' d\sigma(\mathbf{n}') < \infty$, and we have

$$(\mathcal{K}U)(\mathbf{y}, \mathbf{n}) = \int_{\mathbb{R}^3 \times S^2} k(\mathbf{y}, \mathbf{n}; \mathbf{y}', \mathbf{n}') U(\mathbf{y}', \mathbf{n}') d\mathbf{y}' d\sigma(\mathbf{n}'),$$

for almost every $(\mathbf{y}, \mathbf{n}) \in \mathbb{R}^3 \times S^2$ and all $U \in \mathbb{L}_2(\mathbb{R}^3 \times S^2)$. Now $\mathcal{K}_k := \mathcal{K}$ is left-invariant iff k is left-invariant, meaning

$$\forall_{g \in SE(3)} \forall_{\mathbf{y}, \mathbf{y}' \in \mathbb{R}^3} \forall_{\mathbf{n}, \mathbf{n}' \in S^2} : k(g \cdot (\mathbf{y}, \mathbf{n}); g \cdot (\mathbf{y}', \mathbf{n}')) = k(\mathbf{y}, \mathbf{n}; \mathbf{y}', \mathbf{n}').$$

Then to each positive left-invariant kernel $k : \mathbb{R}^3 \times S^2 \times \mathbb{R}^3 \times S^2 \rightarrow \mathbb{R}^+$ with $\int_{\mathbb{R}^3} \int_{S^2} k(\mathbf{0}, \mathbf{e}_z; \mathbf{y}, \mathbf{n}) d\sigma(\mathbf{n}) d\mathbf{y} = 1$ we associate a unique probability density $p : \mathbb{R}^3 \times S^2 \rightarrow \mathbb{R}^+$ by means of $p(\mathbf{y}, \mathbf{n}) = k(\mathbf{y}, \mathbf{n}; \mathbf{0}, \mathbf{e}_z)$. The convolution now reads

$$\mathcal{K}_k U(\mathbf{y}, \mathbf{n}) = (p *_{\mathbb{R}^3 \times S^2} U)(\mathbf{y}, \mathbf{n}) = \int_{\mathbb{R}^3} \int_{S^2} p(R_{\mathbf{n}'}^T(\mathbf{y} - \mathbf{y}'), R_{\mathbf{n}'}^T \mathbf{n}) U(\mathbf{y}', \mathbf{n}') d\sigma(\mathbf{n}') d\mathbf{y}',$$

where σ is the surface measure on S^2 and where $R_{\mathbf{n}'} \in SO(3)$ s.t. $\mathbf{n}' = R_{\mathbf{n}'} \mathbf{e}_z$.

For a proof see [11]. Consequently, the linear scale spaces (9) and (10) are solved by $\mathbb{R}^3 \times S^2$ convolution with the corresponding Green's functions! Next

we extend the ideas in [6,1] and replace the $(+, \cdot)$ -algebra by the $(\max, +)$ -algebra to solve the morphological scale spaces (11) by dilation and erosion on $\mathbb{R}^3 \rtimes S^2$ given by

$$\begin{aligned}(k^- \oplus_{\mathbb{R}^3 \rtimes S^2} U)(\mathbf{y}, \mathbf{n}) &= \sup_{(\mathbf{y}', \mathbf{n}') \in \mathbb{R}^3 \rtimes S^2} [k^-(R_{\mathbf{n}'}^T(\mathbf{y} - \mathbf{y}'), R_{\mathbf{n}'}^T \mathbf{n}) + U(\mathbf{y}', \mathbf{n}')], \\ (k^+ \ominus_{\mathbb{R}^3 \rtimes S^2} U)(\mathbf{y}, \mathbf{n}) &= \inf_{(\mathbf{y}', \mathbf{n}') \in \mathbb{R}^3 \rtimes S^2} [k^+(R_{\mathbf{n}'}^T(\mathbf{y} - \mathbf{y}'), R_{\mathbf{n}'}^T \mathbf{n}) + U(\mathbf{y}', \mathbf{n}')].\end{aligned}\quad (13)$$

where dilation kernels k^- are negative and erosion kernels k^+ are positive.

Definition 2. A viscosity solution of Eq. (11) is a bounded and continuous weak solution $W : (\mathbb{R}^3 \rtimes S^2) \times \mathbb{R}^+ \rightarrow \mathbb{R}$ of (11) such that

1. for any smooth function $V : (\mathbb{R}^3 \rtimes S^2) \times \mathbb{R}^+ \rightarrow \mathbb{R}$ s.t. $W - V$ attains a local maximum at $(\mathbf{y}_0, \mathbf{n}_0, t_0)$ one has $\frac{\partial V}{\partial t}(\mathbf{y}_0, \mathbf{n}_0, t_0) \mp (H(dV(\cdot, \cdot, t)))(\mathbf{y}_0, \mathbf{n}_0) \leq 0$.
2. for any smooth function $V : (\mathbb{R}^3 \rtimes S^2) \times \mathbb{R}^+ \rightarrow \mathbb{R}$ s.t. $W - V$ attains a local minimum at $(\mathbf{y}_0, \mathbf{n}_0, t_0)$ one has $\frac{\partial V}{\partial t}(\mathbf{y}_0, \mathbf{n}_0, t_0) \mp (H(dV(\cdot, \cdot, t)))(\mathbf{y}_0, \mathbf{n}_0) \geq 0$.

with Hamiltonian $H(dV(\cdot, \cdot, t)) = \frac{1}{2\eta} (\mathbf{G}^{-1}(dV(\cdot, \cdot, t), dV(\cdot, \cdot, t)))^\eta$ and with gradient $dV(\mathbf{y}, \mathbf{n}, t) = \sum_{i=1}^5 \mathcal{A}_i V(\cdot, t)|_{(\mathbf{y}, \mathbf{n})} d\mathcal{A}^i|_{(\mathbf{y}, \mathbf{n})}$.

Theorem 2. The unique viscosity solutions of the Hamilton-Jacobi-Bellman equations on $\mathbb{R}^3 \rtimes S^2$, Eq. (11), are resp. given by (+ case) left-invariant erosion

$$W(\mathbf{y}, \mathbf{n}, t) = (k_t^{D^{11}, D^{44}, \eta, +} \ominus_{\mathbb{R}^3 \rtimes S^2} U)(\mathbf{y}, \mathbf{n}) \quad (14)$$

and (- case) left-invariant dilation $W(\mathbf{y}, \mathbf{n}, t) = (k_t^{D^{11}, D^{44}, \eta, -} \oplus_{\mathbb{R}^3 \rtimes S^2} U)(\mathbf{y}, \mathbf{n})$ where $k_t^{D^{11}, D^{44}, \eta, -} = -k_t^{D^{11}, D^{44}, \eta, +}$ and where

$$k_t^{D^{11}, D^{44}, \eta, +}(\mathbf{y}, \mathbf{n}) := \inf_{\substack{\gamma = (\mathbf{x}(\cdot), R(\cdot)) \in C^\infty((0, t), SE(3)), \\ \gamma(0) = (\mathbf{0}, I = R_{\mathbf{e}_z}), \gamma(t) = (\mathbf{y}, R_{\mathbf{n}}), \\ \langle d\mathcal{A}^3|_\gamma, \dot{\gamma} \rangle = \langle d\mathcal{A}^6|_\gamma, \dot{\gamma} \rangle = 0}} \int_0^t \bar{\mathcal{L}}_\eta(\gamma(p), \dot{\gamma}(p)) \left(\frac{dp}{ds} \right)^{\frac{1}{2\eta-1}} dp, \quad (15)$$

with spatial arclength $s > 0$ (of $\mathbf{x}(\cdot)$) and with Lagrangian

$$\bar{\mathcal{L}}_\eta(\gamma(p), \dot{\gamma}(p)) := \frac{2\eta-1}{2\eta} \left(\frac{1}{D^{11}} ((\dot{\gamma}^1(p))^2 + (\dot{\gamma}^2(p))^2) + \frac{1}{D^{44}} ((\dot{\gamma}^4(p))^2 + (\dot{\gamma}^5(p))^2) \right)^{\frac{\eta}{2\eta-1}}$$

with $\dot{\gamma}^i(p) = \langle d\mathcal{A}^i|_{\gamma(p)}, \dot{\gamma}(p) \rangle$ and with $\mathbb{R}^3 \rtimes S^2$ -“erosion arclength” p given by

$$p(\tau) = \int_0^\tau \sqrt{\mathbf{G}_{\gamma(\tilde{\tau})}(\dot{\gamma}(\tilde{\tau}), \dot{\gamma}(\tilde{\tau}))} d\tilde{\tau} = \int_0^\tau \sqrt{\sum_{i \in \{1, 2, 4, 5\}} \frac{|\langle d\mathcal{A}^i|_{\gamma(\tilde{\tau})}, \dot{\gamma}(\tilde{\tau}) \rangle|^2}{D^{ii}}} d\tilde{\tau}. \quad (16)$$

For proof see our technical report [9, App.B]. The Lagrangian in Theorem 2 relates to the Hamiltonian in Def. 2 by Fenchel transform [1] on the Lie algebra of left-invariant vector fields on $SE(3)$, for all $\frac{1}{2} \leq \eta \leq 1$, cf. [9, App.B,ch:8.3].

A *sub-Riemannian manifold* is a Riemannian manifold with the extra constraint that certain subspaces of the tangent space are prohibited. For example, curves in $(SE(3), d\mathcal{A}^1, d\mathcal{A}^2, d\mathcal{A}^6)$ are curves $\tilde{\gamma} : [0, 1] \rightarrow SE(3)$ such that

$$\langle d\mathcal{A}^1|_{\tilde{\gamma}(s)}, \dot{\tilde{\gamma}}(s) \rangle = \langle d\mathcal{A}^2|_{\tilde{\gamma}(s)}, \dot{\tilde{\gamma}}(s) \rangle = \langle d\mathcal{A}^6|_{\tilde{\gamma}(s)}, \dot{\tilde{\gamma}}(s) \rangle = 0, \quad (17)$$

for all $s \in [0, 1]$. Curves satisfying (17) are called *horizontal curves* in $SE(3)$ and we depicted such a curve in Fig. 7.

In [11, ch:6.2] we have analytically approximated the Green's functions of contour completion, Eq. (10) and contour enhancement, Eq. (9) that take place on the sub-Riemannian manifold $(SE(3), d\mathcal{A}^1, d\mathcal{A}^2, d\mathcal{A}^6)$. These Green's functions coincide with the diffusion kernels for respectively the direction process and Brownian motion on $\mathbb{R}^3 \times S^2$ in probability theory, [9, ch:8]. Moreover, in [9, App. A, B, C] we applied similar techniques to approximate the dilation/erosion kernels that describe the growth of balls in the sub-Riemannian manifold $(SE(3), d\mathcal{A}^3, d\mathcal{A}^6)$, cf. Theorem 2. Again there exists a connection with probability theory as these erosion kernels coincide with transition-cost densities of Bellman-processes defined on $(SE(3), d\mathcal{A}^3, d\mathcal{A}^6)$, see [9, ch:8.3].

The next theorem provides some of the *approximations* for the Green's functions, cf. [11, ch:6.2], [9, App.B]:

Theorem 3. *Let $1 \geq \eta > \frac{1}{2}$, $D^{11} > 0$, $D^{33} > 0$, $D^{44} > 0$. Then for the morphological erosion (+) and dilation kernel (-) on $\mathbb{R}^3 \times S^2$ one can use the following approximation*

$$k_t^{D^{11}, D^{44}, \pm}(\mathbf{y}, \mathbf{n}) \approx \frac{(2\eta-1)(c^{-2\eta} t)^{-\frac{1}{2\eta-1}}}{\pm 2\eta} \left(\left(\frac{|c^1|^2 + |c^2|^2}{D^{11}} + \frac{|c^4|^2 + |c^5|^2}{D^{44}} \right)^2 + \frac{|c^3|^2}{D^{11} D^{44}} \right)^{\frac{\eta}{2(2\eta-1)}}$$

for $t > 0$ small, where $\tilde{\mathbf{n}}(\tilde{\beta}, \tilde{\gamma}) = (\sin \tilde{\beta}, -\cos \tilde{\beta} \sin \tilde{\gamma}, \cos \tilde{\beta} \cos \tilde{\gamma})^T$, $c > 0$, with $\tilde{\beta} \in (-\frac{\pi}{2}, \frac{\pi}{2})$, $\tilde{\gamma} \in (-\frac{\pi}{2}, \frac{\pi}{2})$. For the Green's functions of Eq. (9), the heat kernels, we have the approximation

$$p_t^{D^{33}, D^{44}}(\mathbf{y}, \mathbf{n}) \approx \frac{1}{16\pi^2(D^{33})^2(D^{44})^2 t^4} e^{-\sqrt{\frac{|c^1|^2 + |c^2|^2 + |c^6|^2 + \left(\frac{|c^3|^2}{D^{33}} + \frac{|c^4|^2 + |c^5|^2}{D^{44}}\right)^2}{4t}}}.$$

In both cases the functions $c^i := c^i(\mathbf{y}, \tilde{\alpha} = 0, \tilde{\beta}, \tilde{\gamma})$ are given by

$$\begin{aligned} \mathbf{c}^{(1)} &:= (c^1, c^2, c^3)^T = \mathbf{y} - \frac{1}{2} \mathbf{c}^{(2)} \times \mathbf{y} + \tilde{q}^{-2} \left(1 - \left(\frac{\tilde{q}}{2} \right) \cot \left(\frac{\tilde{q}}{2} \right) \right) \mathbf{c}^{(2)} \times (\mathbf{c}^{(2)} \times \mathbf{y}), \\ \mathbf{c}^{(2)} &:= (c^4, c^5, c^6)^T = \frac{\tilde{q}}{\sin(\tilde{q})} \left(\sin \tilde{\gamma} \cos^2 \left(\frac{\tilde{\beta}}{2} \right), \sin \tilde{\beta} \cos^2 \left(\frac{\tilde{\gamma}}{2} \right), \frac{1}{2} \sin \tilde{\gamma} \sin \tilde{\beta} \right)^T \end{aligned}$$

$$\text{with } \tilde{q} = \arcsin \sqrt{\cos^4(\tilde{\gamma}/2) \sin^2(\tilde{\beta}) + \cos^2(\tilde{\beta}/2) \sin^2(\tilde{\gamma})}.$$

For $\eta = \frac{1}{2}$ we obtain the erosion kernel approximation (take $\eta \downarrow \frac{1}{2}$ in Theorem 3):

$$k_t^{D^{11}, D^{44}, \frac{1}{2}, -}(\mathbf{y}, \mathbf{n}) \approx \begin{cases} \infty & \text{if } \sqrt{\left(\frac{|c^1|^2 + |c^2|^2}{D^{11}} + \frac{|c^4|^2 + |c^5|^2}{D^{44}} \right)^2 + \frac{|c^3|^2}{D^{11} D^{44}}} \geq t^2, \\ 0 & \text{else.} \end{cases} \quad (18)$$

The solutions of the pseudo-linear spaces, Eq. (12), are given by

$$W(\mathbf{y}, \mathbf{n}, t) = \chi_C^{-1}((e^{t(D^{33}(\mathcal{A}_3)^2 + D^{44}\Delta_{S^2})} \circ \chi_C \circ U)(\mathbf{y}, \mathbf{n})),$$

i.e. a linear hypo-elliptic diffusion conjugated with the grey-value transformation $\chi_C(I) = \frac{e^{CI}-1}{e^C-1}$ if $C \neq 0$ and $\chi_C(I) = I$ if $C = 0$, $I \in \mathbb{R}^+$, cf. [9, ch], [14].

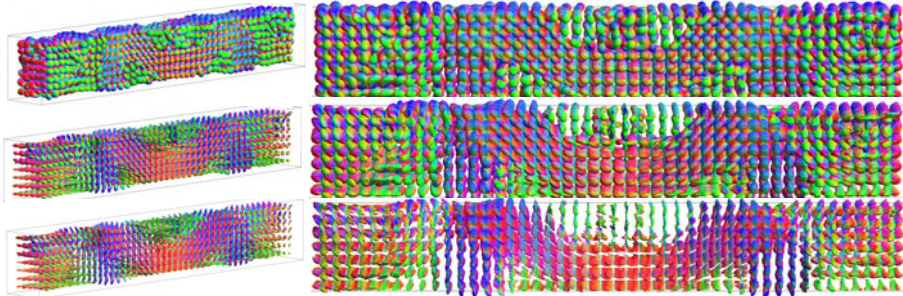


Fig. 8. 1st row: Input DTI-data. 2nd row: Output squared linear diffusion on squared data-set. 3rd row: Output erosion applied to the diffused dataset in the 2nd row.

5 Conclusion

We have developed crossing preserving, rotation- and translation covariant scale spaces on DW-MRI. The underlying evolutions are convection-diffusion equations and Hamilton-Jacobi-Bellman equations of respectively stochastic and cost processes cf. [9], on the space of positions and orientations $\mathbb{R}^3 \times S^2$. These scale spaces are expressed in a moving frame of reference allowing (hypo-elliptic) diffusion along fibers and erosion orthogonal to fibers. They extrapolate complex fiber-structures (crossings) from DTI, while reducing non-aligned crossings in HARDI. They can be implemented by finite difference methods [7] (e.g. Fig. 4 and Fig. 8), or by convolutions with analytic kernels (e.g. Fig. 1 and 2).

References

1. Akian, M., Quadrat, J., Viot, M.: Bellman processes. Lecture Notes in Control and Information Science 199, 302–311 (1994)
2. Alexander, D.C., Barker, G.J., Arridge, S.R.: Detection and modeling of non-gaussian apparent diffusion coefficient profiles in human brain data. Magnetic Resonance in Medicine 48, 331–340 (2002)
3. Basser, P.J., Mattiello, J., Lebihan, D.: MR diffusion tensor spectroscopy and imaging. Biophysical Journal 66, 259–267 (1994)
4. Boscaïn, U., Duplaix, J., Gauthier, J.P., Rossi, F.: Anthropomorphic image reconstruction via hypoelliptic diffusion. (accepted for publication in JMIV, to appear)
5. Burgeth, B., Pizarro, L., Didas, S., Weickert, J.: 3d-coherence-enhancing diffusion filtering for matrix fields. In: Florack, Duits, Jongbloed, van Lieshout, Davies (eds.) Locally Adaptive Filters in Signal and Image Processing (to appear, 2011)

6. Burgeth, B., Weickert, J.: An explanation for the logarithmic connection between linear and morphological systems. In: Griffin, L.D., Lillholm, M. (eds.) Scale-Space 2003. LNCS, vol. 2695, pp. 325–339. Springer, Heidelberg (2003)
7. Creusen, E.J., Duits, R., Dela Haije, T.C.J.: Numerical schemes for linear and non-linear enhancement of DW-MRI. In: Bruckstein, A.M., et al. (eds.) SSVM 2011. LNCS, vol. 6667, pp. 14–25. Springer, Heidelberg (2011)
8. Descoteaux, M.: High Angular Resolution Diffusion MRI: From Local Estimation to Segmentation and Tractography. PhD thesis, Universite de Nice (2008)
9. Duits, R., Creusen, E.J., Ghosh, A., Dela Haije, T.C.J.: Diffusion, convection and erosion on $SE(3)/(0 \times SO(2))$ and their application to the enhancement of crossing fibers. Published on Arxiv, nr. arXiv:1103.0656v4 also available as CASA-report (2011), <http://arxiv.org/abs/1103.0656v4>, <http://www.win.tue.nl/analysis/reports/rana11-22.pdf>
10. Duits, R., Franken, E.M.: Left-invariant parabolic evolutions on $SE(2)$ and contour enhancement via invertible orientation scores, part I: Linear left-invariant diffusion equations on $SE(2)$. Quarterly of Appl. Math., A.M.S. 68, 255–292 (2010)
11. Duits, R., Franken, E.M.: Left-invariant diffusions on the space of positions and orientations and their application to crossing-preserving smoothing of HARDI images. International Journal of Computer Vision, IJCV 92(3), 231–264 (2011), <http://www.springerlink.com/content/511j713042064t35/>
12. Duits, R., van Almsick, M.A.: The explicit solutions of linear left-invariant second order stochastic evolution equations on the 2d-Euclidean motion group (April 2008)
13. Florack, L.: Codomain scale space and regularization for high angular resolution diffusion imaging. In: CVPR Workshop on Tensors in Image Processing and Computer Vision, Anchorage, Alaska, The United States, vol. 20 (June 2008)
14. Florack, L.M.J., Maas, R., Niessen, W.J.: Pseudo-linear scale-space theory. International Journal of Computer Vision 31(2/3), 247–259 (1999)
15. Gur, Y., Sochen, N.: Regularizing Flows over Lie groups. Journal of Mathematical Imaging and Vision 33(2), 195–208 (2009)
16. Mumford, D.: Elastica and computer vision. In: Algebraic Geometry and Its Applications, pp. 491–506. Springer, Heidelberg (1994)
17. Petitot, J.: Neurogéométrie de la vision—Modèles mathématiques et physiques des architectures fonctionnelles. Les Éditions de l’École Polytechnique (2008)
18. Prckovska, V., Rodrigues, P., Duits, R., Vilanova, A., ter Haar Romeny, B.M.: Extrapolating fiber crossings from DTI data. Can we infer similar fiber crossings as in HARDI? In: CDMRI 2010 Proc. MICCAI Workshop Computational Diffusion MRI, China (2010)
19. Rodrigues, P., Duits, R., Vilanova, A., ter Haar Romeny, B.M.: Accelerated Diffusion Operators for Enhancing DW-MRI. In: Eurographics Workshop on Visual Computing for Biology and Medicine, Leipzig, Germany, pp. 49–56 (2010)